Research Article

For reprint orders, please contact: reprints@futuremedicine.com

Nanomedicine

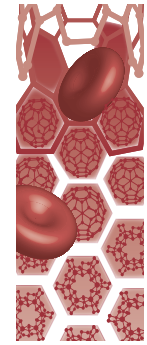

Growth of anisotropic gold nanoparticles in photoresponsive fluid for UV sensing and erythema prediction

Aim: To develop a novel plasmonic nanosensing technique to monitor the exposure levels of UV light for sunlight disease prevention. **Methods:** Anisotropic gold nanoparticles were grown inside a UV photoresponsive fluid, which was previously exposed to UV radiation from different sources. The morphology and optical properties of the obtained nanoparticles were monitored by spectroscopy and microscopy. **Results:** The morphological and optical properties of the nanoparticles were dependent on the UV dose. The UV exposure levels were accurately correlated to the UV minimal doses to produce erythema to different skin types. **Conclusion:** This plasmonic nanosensing technique can be employed as novel sunlight-indexing tool for monitoring the dangerous level of skin exposure.

First draft submitted: 30 April 2016; Accepted for publication: 18 July 2106; Published online: 14 October 2016

Keywords: erythema • gold nanorods • photoresponsive fluid • UV sensor

Roger M Pallares[1,2], Yusong Wang[2], Suo H Lim[2], Nguyễn T K Thanh*[,3,4] & Xiaodi Su**[,2]

[1]Department of Chemistry, University College London, London, WC1H 0AJ, UK

[2]Institute of Materials Research & Engineering, A*STAR (Agency for Science, Technology & Research), 2 Fusionopolis Way, Innovis, #08–03, 138634, Singapore

[3]Biophysics Group, Department of Physics & Astronomy, University College London, London, WC1E 6BT, UK

[4]UCL Healthcare Biomagnetic & Nanomaterials Laboratories, 21 Albemarle Street, London, W1S 4BS, UK

*Author for correspondence: ntk.thanh@ucl.ac.uk

**Author for correspondence: xd-su@imre.a-star.edu.sg

Over the last decade, metallic nanoparticles have captured great scientific attention due to their wide biomedical applications, such as photothermal therapy [1–3], drug delivery [4], imaging [5–8] and sensing [9–11]. Their unique optical and electrical properties rely on the collective oscillation of the electrons in the conduction band called surface plasmon resonance (SPR) [12], which can be customized by changing the nanoparticle size [13] and shape [14]. Due to a great advancement of synthetic methods, a broad range of nonspherical metallic nanoparticles have been obtained, for example, rod [15,16], star [17–19], shell [20,21], prism [22,23], worm [24] and others [25]. Even though each morphology requires a different synthetic route, few of them use hexadecyltrimethylammonium bromide (CTAB) as a main symmetry-breaking component [25]. CTAB is a cationic surfactant that self-assemble in spherical micelles in water [26]. Interestingly, CTAB micelle behavior can be modified by introducing additives such as salts, co-surfactants or organic compounds [27]. Controlling anisotropic gold nanoparticle morphology, particularly gold nanorods (AuNRs), was initially achieved by regulating the presence of silver cations in solution [28]. In recent years, it has been accomplished by modifying the rheological behavior of the surfactant with the addition of organic [29] or inorganic salts [26] into the CTAB-containing growth solution. When a photoresponsive organic compound is added to the CTAB solution, a photorheological fluid can be obtained [30–32]. These smart fluids present light-tunable properties, which we hypothesize can control the growth of anisotropic nanoparticles by irradiating the reaction mixture before the gold reduction takes place. Previously, the photochemical synthesis of AuNRs had been accomplished by a different principle, that is, introducing acetone into the growth solution and irradiating it with UV light for 30 h [33]. Although the mechanism is still not clear, it has been suggested that acetone acts as catalyst in the gold reduction [34]. Later, the long

Future Medicine part of fsg

reaction time was improved by combining a chemical reduction step with the photoirradiation [35]. However, this double-reduction procedure did not yield the larger rods with the longer irradiation time. The rod aspect ratio initially increased with the irradiation time until reaching a maximum, after which the rod length started to decrease.

Gold nanoparticles have been abundantly used in colorimetric sensing, due to their strong extinction coefficients in the visible and near-infrared wavelength range [9]. Traditional approaches measure the shift of the SPR band as a consequence of the analyte-induced nanoparticle aggregation. Those sensors can be generally classified under cross-linking [36–39] or noncross-linking (i.e., electrostatic) principles [40–42], depending on the aggregation driving force. Nevertheless, these sensors using as-prepared nanoparticles present several drawbacks such as complex post-synthesis surface modifications in the case of cross-linking-based sensors and weak binding interactions, which may be impaired by the buffer or the medium-containing species, and low specificity in the case of noncross-linking-based sensors. Therefore, recent efforts have been made in order to develop a totally new analytical approach, where the nanoparticles are not synthesized beforehand and later exposed to the analyte, but synthesized in the presence of the analyte, and their growth is driven by the analyte concentration that is termed as *in situ* growth sensing. So far the most successful design of such system is the gold nanoparticle-based ELISA for cancer markers developed by de la Rica *et al.* [43]. In this design, nonaggregated spherical or aggregated nonspherical gold nanoparticles are produced under enzymatic interaction, depending on the prostate-specific antigen or p24 levels. Since its publication, this sensing principle has been further applied to other biomarkers [44,45]. Coronado-Puchau *et al.* were able to correlate the growth of AuNRs to the levels of a nerve gas analogue by enzymatically quenching the nanorod growth [46]. Even though these designs that combine the synthesis and sensing in a single step are superior than the traditional approaches, they all rely on enzyme-based signal generation, which increases the design complexity and experimental times.

Nanotechnology and nanosensing have the potential to benefit several biomedical fields such as sunlight-related disease prevention [47]. The impact of UV radiation (UVR) on human health has become a major concern according to WHO, due to the strong increase in skin cancer incidence and ozone depletion over the last decades [48]. The exposure of skin to solar UVR produces erythema [49], a skin inflammation commonly known as 'sunburn'. The UVR damages the epidermal DNA, mostly producing pyrimidine dimers [50]. Those lesions are premutagenic and have been linked to many UV-related diseases, such as immunosuppression [50]. Even though the DNA integrity is generally restored by repair processes and the damaged cells are eliminated by apoptosis [51], the malfunction of those mechanisms may lead to melanoma [52]. Nevertheless, an opposite health issue related to the lack of UV exposure has recently emerged as widespread threat, that is, vitamin D insufficiency, which is directly linked to several bone disease, such as rickets and osteomalacia [53]. Therefore, novel and inexpensive systems capable of measuring human exposure to UV are required.

In this work, we study the effect of growing anisotropic gold nanoparticles, that is, nanorods and nanoworms, in a photoresponsive medium. We demonstrate that the UV irradiation induces physical and chemical changes on the growth solution, which ultimately controls the nanoparticle dimensions. Furthermore, we apply those UV-depending syntheses as enzyme-free *in situ* growth sensors for solar UVR exposure and erythema prediction.

Materials & methods

Materials

The following products were used as received. Hydrogen tetrachloroaurate ($HAuCl_4$; 99.99% trace metals basis, 30 wt% in dilute HCl), silver nitrate ($AgNO_3$; 99%), hydrogen chloride (HCl; 37% wt in water), L-ascorbic acid (crystalline), sodium borohydride ($NaBH_4$; 98%), *ortho*-methoxycinnamic acid (OMCA, predominantly *trans*, 98%) and dimethyl sulfoxide-d_6 (DMSO-d_6) were purchased from Sigma-Aldrich (UK). CTAB (>98%) and *cis-ortho*-methoxycinnamic acid (99%) were purchased from Tokyo Chemical Industry (Japan).

All the water employed in the experiments was obtained with a Milli-Q Integral 5 system (Merck Millipore, USA).

Sample irradiation

UV irradiations

A total of 7.5 ml solutions made of CTAB (133.3 mM) and *trans*-OMCA (6.7 mM) and contained in sealed glass vials were irradiated in a 400 W UV chamber (DYMAX light curing system, Model 2000 Flood, Dymax Corporation, USA) with maximum irradiation from 300 to 450 nm. The irradiations were carried in air atmosphere.

Solar-simulated irradiations

Solutions with the same composition as in the UV irradiation were irradiated in a 400 W solar simulator (SOL 2 unit, Honle UV Technology, Germany). The irradiations were carried in air atmosphere.

Synthesis of AuNRs

Synthesis of seeds

The reaction was performed at 23°C. The CTAB solution (5 ml, 0.2 M) was added to a 5.0 ml solution of $HAuCl_4$ 0.5 mM. While the mixture was being vigorously stirred, 0.6 ml of ice-cold $NaBH_4$ 10 mM were added at once. The seed solution was stirred for 30 s and was left undisturbed for 1 h. Then, the seeds were immediately used to synthesize the gold nanorods.

Synthesis of rods

A total of 250 µl of $AgNO_3$ (4 mM) were added to the previously irradiated solution (7.5 ml, 133.3 mM CTAB and 6.7 mM *trans*-OMCA). The solution was kept undisturbed for 15 min, after which 2.5 ml of $HAuCl_4$ (2 mM) were added. After slow stirring, ascorbic acid (60 µl, 79 mM) was introduced into the growth solution, which lost its orange color and yielded a colorless solution, because of the reduction of Au^{3+} to Au^{1+}. The mixture was vigorously stirred for 30 s and 60 µl of the seed solution were added. Finally, the growth solution was vigorously stirred for 30 s and left undisturbed for 12 h. The gold nanorods were isolated by centrifugation at 8000 rpm for 15 min followed by removal of the supernatant twice. The precipitate was redispersed in 10 ml of Milli-Q water.

Synthesis of AuNWs

The reaction was performed at 23°C. A total of 70 µl of freshly prepared NaOH (1 M) were added to the irradiated solution (7.5 ml, 133.3 mM CTAB and 6.7 mM *trans*-OMCA) under vigorous stirring. A total of 2.5 ml of $HAuCl_4$ (1 mM) were immediately introduced into the growth solution, changing the color solution to pale yellow. While keeping the vigorous stirring, ascorbic acid (34 µl, 79 mM) was added, yielding a colorless solution. The loss of the color was followed by the addition of 250 µl of $AgNO_3$ (4 mM). The final solution was stirred for 30 s and left undisturbed for 12 h. A fast change in the color from colorless to dark red-brown occurs few minutes after the addition of the last reagent, indicating the formation of gold nanoworms (AuNWs), which were isolated by centrifugation at 7000 rpm for 10 min followed by removal of the supernatant twice. The precipitate was redispersed in 10 ml of Milli-Q water.

Simulated sunlight calculations

The solar-simulated irradiance was measured with a solar meter (DAYSTAR DS-05 model; Daystar, Inc., USA) and optical filters. The UV solar-simulated irradiance of the lamp is 73 W/m^2, which is in good agreement with the ASTM-G173 standard, that is, UV Sun irradiance of 63 or 91 W/m^2 depending if considering diffusion radiation [54]. The nonerythemally weighted UV radiant exposure (J/m^2) was calculated by integrating irradiance over exposure times. For erythemally weighted, the solar-simulated irradiance was decomposed in single irradiances for every wavelength by assuming that the solar lamp and sun irradiances have the same wavelength profile. The global sun irradiance from ASTM-G173 standard was used as a reference. The erythemally weighted irradiance was calculated by applying the Commission Internationale de l´Eclairage (CIE)-standard erythemal weight function to the lamp irradiance. Finally, the irradiance was integrated over time to obtain the erythemally weighted exposure.

Characterization

Transmission electron microscopy (TEM) images and high-resolution TEM (HR-TEM) images were obtained with a JEM-2100 microscope operating at 200 kV. The optical extinction spectra were recorded using a Spectramax M2/M2^e UV/Vis/NIR spectrophotometer. The growth of the nanoparticles was studied with a Cary 60 UV-Vis from Agilent Technologies. The dynamic light scattering (DLS) measurements were performed with a Zetasizer Nano Z from Malvern Instruments. The x-ray diffraction (XRD) measurements were performed with D8 Discover Gadds. pH measurements were recorded with an Orion Star A111 Benchtop meter from Thermo Scientific. The IR spectra were acquired from solid samples with an Fourier transform IR (FTIR) spectrometer (Perkin Elmer Spectrum 2000 with Autoimage). The samples were irradiated in ethanol, dried and grinded with potassium bromide, followed by film pelletization before the measurements. The ^{1}H-NMR spectra were collected with a Bruker DRX 400 MHz.

Results & discussion

Growth of AuNRs

AuNRs are commonly synthesized by seed-mediated methods, where gold salts are reduced in the presence of a cationic surfactant (i.e., CTAB) and small gold nanoparticles that act as seeds [28,55]. When a photosensitive organic acid or salt, which photoisomerizes, is added into a CTAB solution, the organic molecules interact differently depending on the isomer geometry, providing distinctive rheological properties [30–32]. OMCA is one of the rare cases, where its photoisomerization (from *trans* to *cis* form, Figure 1) is irreversible and the rheological changes are only one way and triggered by the absorption of UV light [32].

The effect of UVR on the growth of AuNRs in a photoresponsive fluid, made of CTAB and *trans*-OMCA (final concentrations of 100 and 5 mM, respectively),

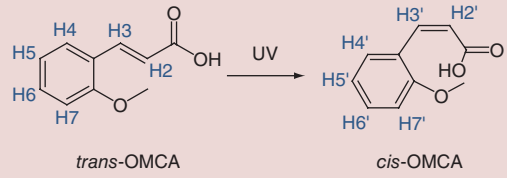

Figure 1. Photoisomerization of ortho-methoxycinnamic acid from *trans* to *cis* form.

has been studied. The growth of AuNRs following the traditional seed-mediated protocol requires acidic conditions [28], which hinders the solubility of OMCA in water. A concentration of 5 mM was found to be optimal, since bigger amounts of OMCA precipitated over time. Identical solutions were irradiated with UV light for different exposure times, before being used in the synthesis of the nanoparticles. The TEM images of the rods grown in those solutions are presented in Figure 2A. Even though the aspect ratio of AuNRs increases from

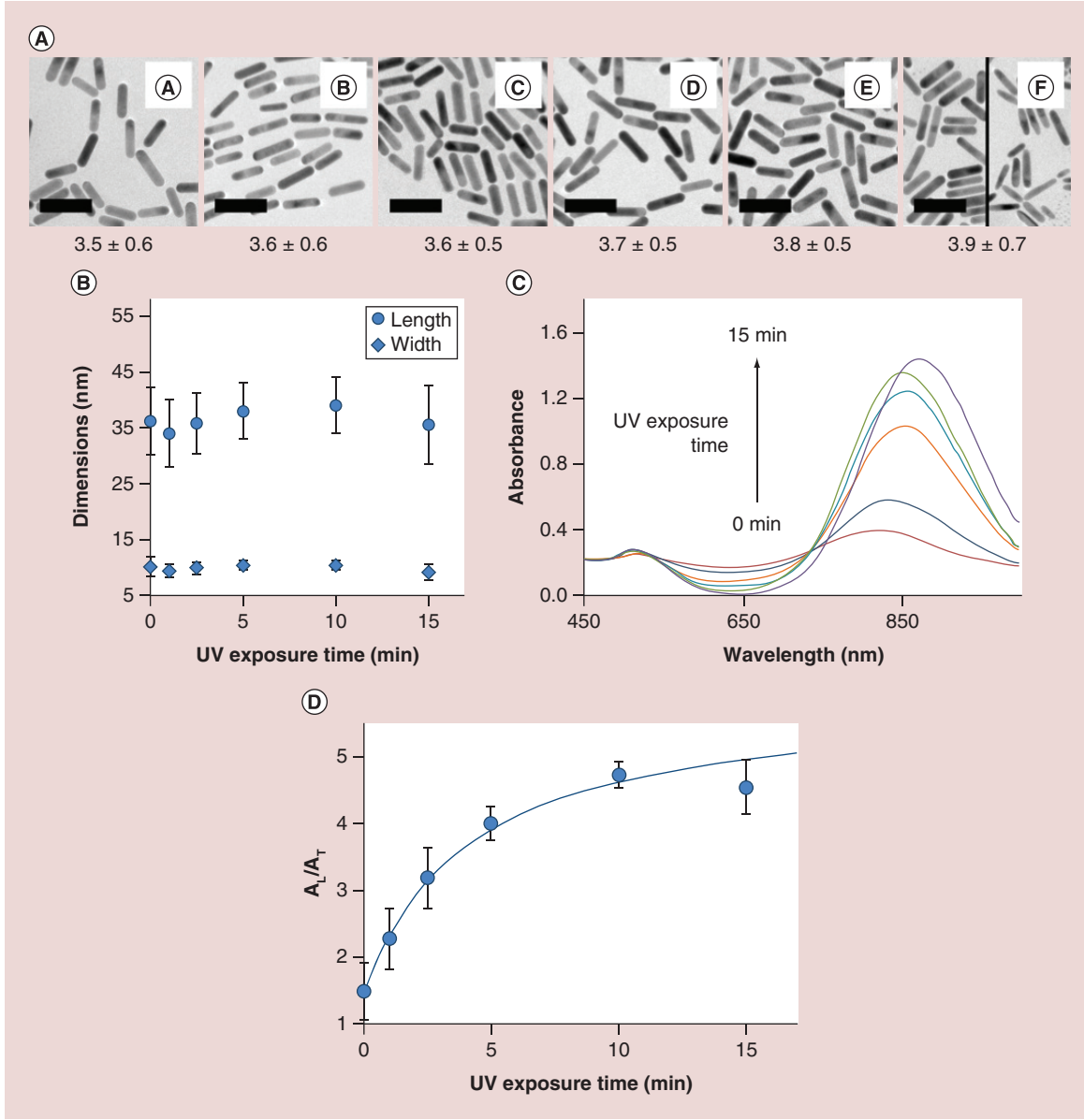

Figure 2. **(A)** TEM images of AuNRs grown in the photoresponsive fluid after UV irradiation for **(a)** 0, **(b)** 1, **(c)** 2.5, **(d)** 5, **(e)** 10 and **(f)** 15 min. AuNR aspect ratios are displayed below the TEM images. Scale bars represent 50 nm. **(B)** Plot of the length and width of the grown AuNRs. **(C)** Corresponding absorbance spectra of the AuNRs. **(D)** Variation of the ratio between the A_L and A_T LSPR bands as a function of UV exposure time. A_L: AuNR longitudinal; A_T: AuNR transversal; LSPR: Localized surface plasmon resonance; TEM: Transmission electron microscopy.

3.5 to 3.9 with increasing UVR, the length and the width do not follow a clear tendency with the exposure time (Figure 2B). Interestingly, AuNRs obtained after 15 min of irradiation present two different populations. One made of bigger rods (38.0 ± 6.0 × 9.8 ± 1.0 nm) and the other composed of rice-shaped rods (31.8 ± 7.2 × 8.0 ± 1.2 nm) with aspect ratios of 3.9 ± 0.6 and 4.0 ± 0.7, respectively. This may suggest a complex combination of phenomena that results on the tuning of the AuNR aspect ratio. The underlying mechanism is thoroughly discussed in the 'Insights Into the Growth Mechanism and the Role of OMCA' section of this paper. The statistical significance of the different aspect ratios has been evaluated by Welch's t-tests (Supplementary Table 1) and the effect size (i.e., standardized measure of the strength of the effect) by Cohen's *d* calculations (Supplementary Table 2). These analyses show the aspect ratio of the rods increase with a precision of 0.1 for the range between 3.5 and 3.9 with small Cohen's *d* values ($0.16 \leq d \leq 0.20$) but statistical significance ($p < 0.05$). In other words, even though the effect of the UVR on the aspect ratio is small, it is statistically significant. The change of the rod morphology contributes to increase and shift of the longitudinal localized SPR (L-LSPR) band from 813 up to 862 nm (Figure 2C). Figure 2D presents the intensity ratio between the two LSPR bands (AuNR longitudinal [A_L]/AuNR tranversal [A_T]) of the AuNRs grown after different irradiation times. The ratio values shift from 1.4 to 4.7 with increasing UVR times, and saturation is reached after 10 min of irradiation. It is important to note that the strong shift of A_L/A_T by UVR suggests that the variation of the AuNR's optical properties can be used as transducer signal for robust UV sensing. Nevertheless, the L-LSPR bands in all the nanoparticle solutions are in the near-IR region, outside of the visual spectrum. Thus, those changes are not detectable by naked eye and require UV-Vis spectrometer as quantitative detection system.

The growth kinetics of the rods was studied by UV-Vis spectroscopy. Figure 3A presents the evolution of AuNR growth in the presence of 5 mM *trans*-OMCA. A wide plasmon band appears around 720 nm after 6 min of reaction. It redshifts and its intensity increases as the reaction progresses. The growth of the AuNRs is completed after 16 min and no further changes are observed in the spectrum. Interestingly, standard protocols for the synthesis of AuNRs (i.e., in absence of *trans*-OMCA) require higher amounts of ascorbic acid, which is the essential reagent for the gold reduction. OMCA presents mild reducing behavior, which may play a role in the reduction of gold salts. Therefore, we compared the AuNR growth kinetics in the presence and absence of *trans*-OMCA. Figure 3B shows the intensity ratio between the two AuNR LSPR bands (A_L/A_T) against the experimental time.

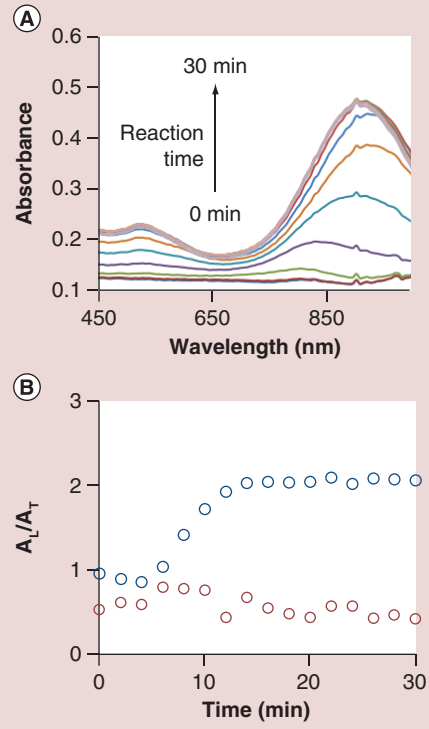

Figure 3. (A) Absorbance spectra of the AuNRs grown in the photoresponsive fluid over the time. **(B)** Correlation between the intensity ratio of the A_L and A_T LSPR bands with reaction time in the presence (blue) and absence (red) of 5 mM *trans*-OMCA. The UV irradiation time is 0 min.
A_L: AuNR longitudinal; A_T: AuNR transversal; LSPR: Localized surface plasmon resonance; OMCA: *Ortho*-methoxycinnamic acid.

In the presence of *trans*-OMCA, AuNR growth takes 16 min to complete, as previously described. On the other hand, AuNRs do not grow in the absence of *trans*-OMCA. We hypothesize that *trans*-OMCA contributes to the gold reduction, and ascorbic acid at 79 mM (60 µl) by itself is not enough to reduce the gold salts to metallic gold. It is worth mentioning that several aromatic compounds have been reported reducing gold salts in the formation of gold nanoparticles [56–59]. To confirm this hypothesis, a growth solution (containing 0.5 mM $HAuCl_4$) was left undisturbed without adding ascorbic acid and seeds. Supplementary Figure 1A shows the slow reduction of Au^{3+} to Au^{+} in the presence of *trans*-OMCA. Au^{+} is not further reduced to metallic gold, as observed by the absence of plasmon band. Interestingly, *trans*-OMCA requires significantly larger times to reduce Au^{3+} to Au^{+} than ascorbic acid, that is, 10 h and few seconds, respectively. AuNR growth and gold reduction kinet-

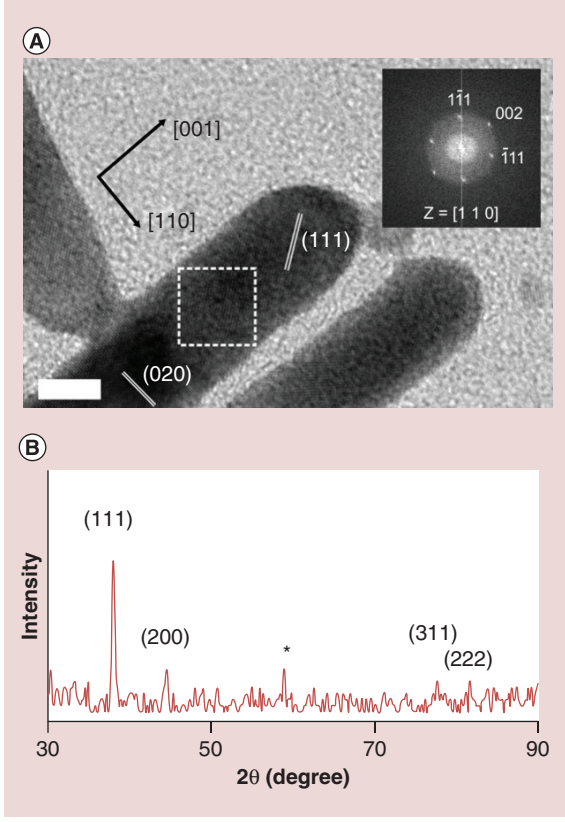

Figure 4. (A) HR-TEM image of AuNRs synthesized in the photoresponsive fluid. The inset in the image is the fast Fourier transform pattern of the selected region. Scale bar represents 5 nm. **(B)** XRD pattern of AuNRs obtained in the photoresponsive fluid. Asterisk denotes a substrate peak (Si (444)) [60]. The UV irradiation time is 0 min.
HR-TEM: High resolution-transmission electron microscopy; XRD: X-ray diffraction.

ics suggest that even though *trans*-OMCA's contribution to reduce the gold salts is very small, it is essential for the final growth of the rods.

Finally, the crystalline structure of the nanoparticles was characterized. HR-TEM images indicate that the rods are single-crystal, growing along the [001] direction (Figure 4A). The analysis of the fast Fourier transform obtained from the HR-TEM images shows face-centered cubic spot pattern, acquired along the [110] zone axis. Furthermore, the XRD patterns present strong peaks at (111) and (200), which are coherent with metallic gold (Figure 4B).

Growth of AuNWs

The reducing behavior of ascorbic acid is pH-dependent [61]. When the pH of the growth solution is increased (pH ≈ 11), ascorbic acid can completely reduce Au^{3+} to Au^{0} without the presence of seeds. Due to the fast reduction kinetics, CTAB cannot efficiently break the nanoparticle symmetry and effectively induce the growth of AuNRs [62]. Nevertheless, twisted gold nanowires (i.e., AuNWs) can be formed at that basic pH under highly controlled conditions [24]. It has been proposed that CTAB's higher affinity for {100} and {110} facets induces an anisotropic coverage of the newly formed nanoparticles, originating electrostatic interactions among them and promoting their oriented attachment [24]. The deposition of reduced gold on top of those assembled nanoparticles yields the final AuNWs.

To study the growth of AuNWs in a photoresponsive fluid, several solutions with same composition (i.e., final concentration of 100 mM CTAB and 5 mM *trans*-OMCA) were exposed to UVR for different times. Those solutions were lately used to synthesize the AuNWs shown in Figure 5A. The aspect ratio of the worms decreases from 5.5 to 3.9 upon 15 min of irradiation. Interestingly, this is the opposite phenomenon that the one observed for AuNRs, where their aspect ratio increases with UVR. Those variations of the aspect ratio are statistically significant ($p < 0.05$; Supplementary Table 3) with big Cohen's d values ($d \geq 1.00$; Supplementary Table 4).

Both length and width decrease upon UVR exposure, from 137.4 to 71.2 nm and from 25.0 to 18.2 nm, respectively (Figure 5B). Due to the decrease in the aspect ratio, the L-LSPR band shifts from above 995 to 800 nm (Figure 5C).

The growth of AuNWs studied by UV-Vis spectroscopy presents two clear phases. The first one is the fast formation of a broad plasmon band around 500 nm, which indicates the growth of gold nanocrystals above 2 nm in size [63], and small L-LSPR band within the first 2 min of reaction (Figure 6A). In a second phase, the AuNWs start growing, as indicated by the increase of both plasmon bands, in a slower process that lasts around 83 min (Figure 6B). It is worth mentioning, that the appearance of the first plasmon band is significantly faster in the case of AuNWs than in the AuNRs, being 30 s and 6 min, respectively. Nevertheless, the total growth time for AuNRs is shorter than the one for AuNWs, being 16 and 85 min, respectively. This observation suggests that, although the initial formation of nanoparticles in the AuNW synthesis is fast, the nanoparticle-oriented attachment and further gold deposition on top of them is a remarkably slower process.

In the previous section we proved that OMCA presents a pivotal role in the reduction of gold salts in AuNR synthesis, together with ascorbic acid. Here, we performed the same study under AuNW growth conditions (Supplementary Figure 1B). We found that total reduction of Au^{3+} to Au^{+} occurs after 15 min of reaction in absence of ascorbic acid. This is significantly faster than the reduction occurred under AuNR growth

conditions (i.e., 10 h). We hypothesize that the faster reduction kinetics is the result of two factors: stronger reducing power of OMCA at higher pH (i.e., cinnamic acid family presents stronger reducing capabilities at higher pH) [64–66]; the lower concentration of Au^{3+} in solution. Nevertheless, same as observed for AuNR synthesis, *trans*-OMCA is insufficient to completely reduce gold salts to metallic gold, and nanoparticles do not grow in solution. This is confirmed by the absence of plasmon band around 500 nm.

Another important information concerning the AuNW growth is observed in the TEM images (Figure 7A). As Ahmed *et al.* had previously reported [24], AuNWs present distinguishable domains, which are most likely formed from the attachment of different nanoparticles. HR-TEM images show that the different domains present indeed different crystal orientation (Supplementary Figure 2). The nanoworm polycrystallinity is further confirmed by the ring structure in the fast Fourier transform obtained from the HR-TEM images (Figure 7B). Finally, the XRD pattern is coherent with the electron diffraction pattern, showing two strong peaks at (111) and (200) and three smaller at (220), (311) and (222), which are characteristic of metallic gold (Figure 7C).

Insights into the growth mechanism & the role of OMCA

The experimental results of the previous sections prove that UV light can affect the morphology of anisotropic gold nanoparticles grown in a photoresponsive fluid. In this section we list the main observations that will lead to the understanding of the mechanism behind this phenomenon.

First, OMCA photoisomerization was characterized by UV-Vis spectroscopy. Figure 8 presents the spectra of solutions containing 100 mM CTAB and 5 mM *trans*-OMCA after irradiation with UV light. The two absorbance peaks blueshift and their absorbance intensities decrease upon irradiation, indicating that the photoisomerization from *trans* to *cis* occurs. Interestingly, not all *trans*-OMCA are converted to their *cis* isomer, and the photostationary equilibrium is reached when around 83% of all OMCA molecules are in *cis* form. This is in agreement with previous literature values [32]. The spectra of both isomers were also recorded in absence of CTAB and similar results are observed (Supplementary Figure 3). FTIR and NMR spectroscopies were used to further characterize the photoisomerization. The FTIR spectra of *trans* (after being irradiated with UV light for 0, 5, 10 or 15 min)

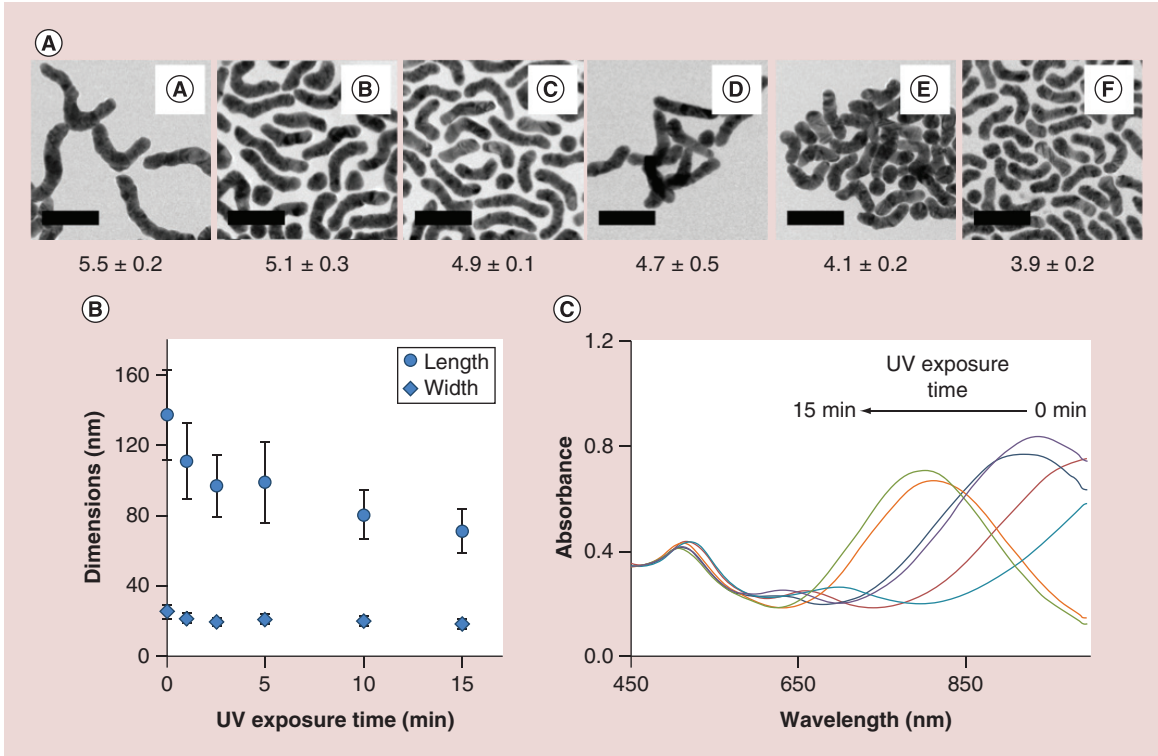

Figure 5. (A) TEM images of AuNWs grown in the photoresponsive fluid after **(a)** 0, **(b)** 1, **(c)** 2.5, **(d)** 5, **(e)** 10 and **(f)** 15 min of UV irradiation. AuNW aspect ratios are displayed below the TEM images. Scale bars represent 100 nm. **(B)** Plot of the length and width of grown AuNWs. **(C)** Absorbance spectra of AuNWs grown in the photoresponsive fluid after 0, 1, 2.5, 5, 10 and 15 min of UV irradiation.
TEM: Transmission electron microscopy.

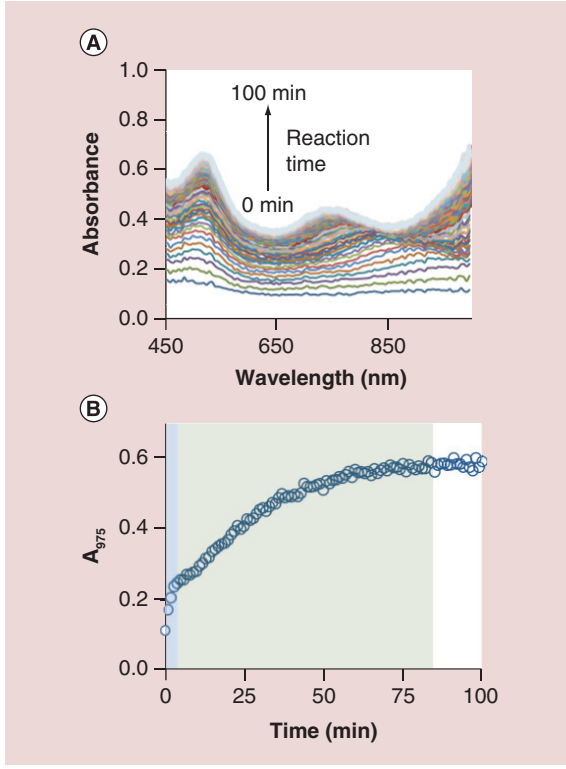

Figure 6. (A) Absorbance spectra of the AuNWs grown in the photoresponsive fluid over the time (from 0 to 100 min). **(B)** Correlation between the absorbance intensity at 975 nm against reaction time. The two phases of AuNW growth, that is, fast formation of the plasmon bands and their slow increase, are highlighted in blue and green, respectively. The UV irradiation time is 0 min.

and *cis*-OMCA were acquired. *Trans* and *cis* isomers can be distinguished by the position of their acrylic out-of-plane =C-H bending bands (γ=C-H) [67], which are located at 879 [68] and 837 cm^{-1} [69], respectively.

In addition, *cis*-OMCA presents a characteristic ring breathing band around 793 cm^{-1} [69]. Figure 9A shows the decrease of the band at 879 cm^{-1} and the increase of both 837 and 793 cm^{-1} bands with increasing UVR time. Furthermore, *trans*-OMCA presents a characteristic aromatic C-H in-plane bending vibration (βC-H) located at 996 cm^{-1} [68], which decreases with the UVR. All those results are coherent with photoisomerization *trans* to *cis*. There are changes in other characteristic bands that are also consistent with photoisomerization. The samples' irradiation increases the two strong C-C stretching vibrations (sC-C) at 1291 and 1246 cm^{-1} associated to *cis*-OMCA [69], while the two less-intense bands at 1302 and 1202 cm^{-1} linked to *trans*-OMCA [68] decrease in intensity. It is worth mentioning that all spectra present the characteristic bands of the acrylic C=C vibration (*v*C=C) at 1622 cm^{-1} for *trans* [68] or at 1639 cm^{-1} for *cis*-OMCA [69]. The existence of those *v*C=C vibrations confirms that UVR does not induce photodimerization [70]. The ^{1}H-NMR spectra of *trans* (before and after being irradiated for 15 min) and *cis*-OMCA in DMSO-d_6 were also collected (Figure 9B) to complement the FTIR studies. The ^{1}H chemical shifts are summarized in Table 1 and assigned on the basis of theoretical estimations (performed with the commercial Chemdraw Ultra software, PerkinElmer, USA) and literature values of related cinnamic compounds [71]. The main difference between the two isomers is the peak positions of the acrylic hydrogens, which are located at 6.54 (H2) and 7.86 pm (H3) for *trans* and 5.97 (H2') and 7.02 pm (H3') for *cis*-OMCA. After 15 min of UVR, *trans*-OMCA spectrum presents peaks from both isomers, with the stronger ones associated to the *cis* form. This suggests that the photoisomerization has occurred but it was incomplete. An isomerization yield of 80% is calculated by integrating the signal intensities. This value is in agreement with the yield previously calculated from the UV-Vis data (i.e., 83%).

Second, *trans* and *cis* isomers of cinnamic acid derivates are known to present distinctive physical and chemical properties, such as pKa [72,73] or freezing point [74]. Those differences are due to the conjugation between the double bound and the aromatic ring, which is sterically hindered in the *cis* forms [75]. Furthermore, *trans*-OMCA presents stronger association with CTAB micelles than the *cis* isomer, most likely due to its geometry and higher hydrophobicity [32]. Therefore, the effect of UV light on the nanoparticle tuning has to be analyzed from two different points of views, that is, changes on the interaction between surfactant and OMCA, and changes on the growth solution conditions triggered by the isomerization.

Third, ascorbic acid presents two pKa, one at 4.04 [76] (i.e., transition from protonated form to ascorbate monoanion) and the other at 11.34 [77] (i.e., transition from ascorbate monoanion to dianionic form). It is generally accepted that the reducing behavior of ascorbic acid increases from protonated to dianionic form [78–80]. Thus, its antioxidant strength increases with the pH, as stronger reducing species are produced in the medium. The pH of the growth solution was studied for different UV irradiation times before the addition of ascorbic acid and seeds. For AuNR growth solutions, the pH decreases from 3.06 to 3.01 after 15 min of irradiation (Supplementary Table 5). The *trans* isomers of cinnamic acid family have higher pKa than that of the *cis* forms [72,73]. Therefore, the photoisomerization produces more acidic species, which decrease the solution's pH. The higher acidity of *cis*-OMCA isomer was confirmed by comparing the pH of the solutions of the two isomers at 1 mM

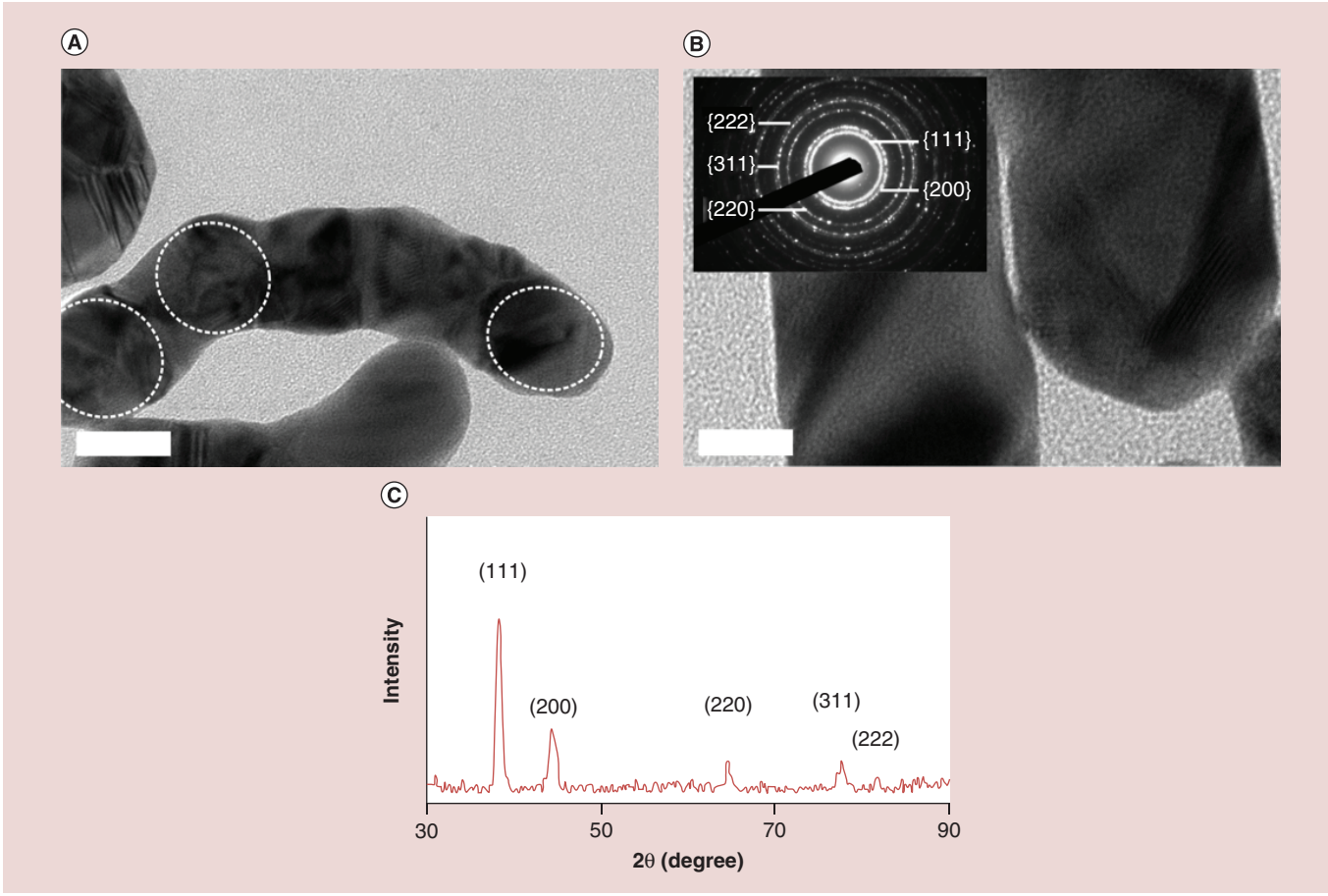

Figure 7. (A) TEM image of the AuNWs. The circles highlight the areas of different domains. Scale bar represents 10 nm. **(B)** HR-TEM image of AuNWs synthesized in the photoresponsive fluid. The inset in the image is the fast Fourier transform pattern of the AuNW. Scale bar represents 5 nm. **(C)** XRD pattern of AuNWs obtained in the photoresponsive fluid. The UV irradiation time is 0 min. HR-TEM: High resolution-transmission electron microscopy; TEM: Transmission electron microscopy; XRD: X-ray diffraction.

(Supplementary Figure 3). The decrease of pH reduces ascorbic acid's reducing strength, slowing the growth of the rods. Smaller reducing capacity has been proved to be a key parameter to obtain larger aspect ratio AuNRs [62]. In the case of AuNW growth solutions, the UV irradiation increases the pH from 10.90 to 11.03 (Supplementary Table 5), which contributes to faster gold reduction and shorter aspect ratio worms. Even though it is not clear why the UV irradiation increases the pH in AuNW growth solutions, we hypothesize that may be the result of a complex combination of changes induced by the photoisomerization (e.g., isomer's solubility [32] and redox potential [72,73]) and the solution's high pH (e.g., decrease on the stability of cinnamic acid derivatives [81]).

Fourth, another property that changes between isomers is their reduction and oxidation behavior [82]. Previously, we proved that OMCA contributes to reduce gold salts in the photoresponsive synthesis. Thus, a change on the OMCA reduction potential can affect the growth of the nanoparticles. The reduction behavior of both OMCA isomers was studied under AuNR and AuNW growth conditions. Supplementary Figure 1A presents the Au^{3+} reduction kinetics in the AuNR growth solution (pH ≈ 3) by the action of both isomers. *cis*-OMCA presents faster reduction kinetics than *trans*. Therefore, photoisomerization from *trans* to *cis*-OMCA promotes faster gold reduction and contributes to obtain shorter rods. On the other side, the Au^{3+} reduction kinetics in the AuNW growth solution (pH ≈ 11) are very similar for both isomers (Supplementary Figure 1B) and no major differences are expected in the AuNW growth.

Fifth, OMCA geometry affects the molecular packing of the CTAB/OMCA system and the final micelle morphology. Micelle-shape transitions, such as worm-like to shorter rod micelles, have been obtained by irradiating a solution containing CTAB and *trans*-OMCA (i.e., 60 and 50 mM, respectively) with UV light [32]. Recently, it has been proved that CTAB micelle morphology affects the growth of AuNRs and their final aspect ratio [26]. Based on those observa-

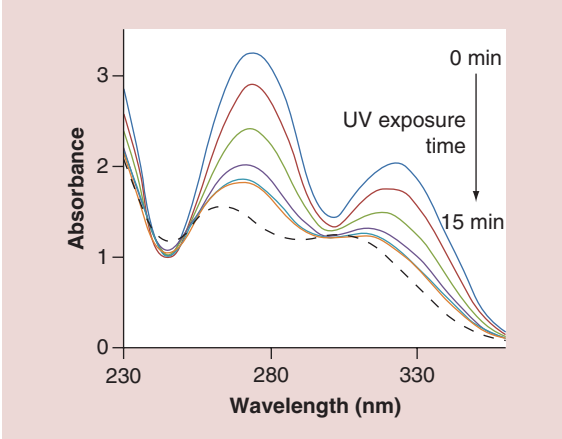

Figure 8. Absorbance spectra of trans-ortho-methoxycinnamic acid (in a solution made of 100 mM hexadecyltrimethylammonium bromide and 5 mM *trans-ortho*-methoxycinnamic acid) after being irradiated with UV light for 0, 1, 2.5, 5, 10 and 15 min. The spectrum of *cis*-OMCA (dashed line) is plotted for reference.
OMCA: *Ortho*-methoxycinnamic acid.

tions, we studied if the UV light induces changes on CTAB micelle morphology, which could explain the nanoparticle tuning. Supplementary Table 6 presents the hydrodynamic diameter of CTAB micelles in the growth solutions measured by DLS. The micelle sizes are constant and independent of the irradiation time, with no morphological changes (i.e., size or shape) detectable by DLS. Nevertheless, AuNR and AuNW growth solutions present different micelle size, 0.9 and 1.5 nm, respectively. This size difference is likely due to the different pH. Aromatic counterions interact with CTAB micelles by inserting the aromatic ring in the surfactant aliphatic chain, while keeping the anionic part between the polar heads [27]. This decreases the electrostatic repulsion between the CTAB polar heads, bringing the surfactant molecules closer and inducing the growth of the micelle. The OMCA pKa is 4.70 [83]. Thus, higher concentration of anionic OMCA is produced at pH ≈ 11 than 3 (i.e., growth condition for AuNW and AuNR synthesis, respectively). Since, anionic OMCA can strongly screen the electrostatic repulsion between CTAB polar heads, AuNW growth solutions present larger micelles.

In conclusion, OMCA presents four key characteristics: it is photoresponsive; OMCA isomers have different redox behavior; it affects the pH of the solution; and it has a structural role in forming the CTAB micelles. Table 2 summarizes the mechanistic observations described in the previous paragraphs. The increase of pH under AuNW growth conditions, promotes shorter aspect ratio worms. Both isomers present similar reduction behavior at those conditions, thus the nanoworm aspect ratio decreases upon UVR. On the other hand, UV light decreases the pH under AuNR growth conditions, promoting larger aspect ratio rods. However, the photoisomerization of *trans*-OMCA yields *cis* isomer, which presents stronger reduction behavior at that pH and contributes to shorter rods. The two factors confront and promote opposing results. This may explain why AuNRs are tuned in a significantly narrower range than that for AuNWs, with L-LSPR band shifts of 49 and above 195 nm, respectively. Nevertheless, the changes on the pH seem to be more significant than the OMCA-reduction behavior. This can be rationalized since the pH affects the redox potential of ascorbic acid, which is the main reducing reagent in the reaction. Finally, the micelle packing does not change by the photoisomerization and it does not play a role on the nanoparticle tuning.

In situ growth sensing of UV radiant exposure for erythema prevention

For sensing applications, UV exposure can be measured as received (i.e., without any mathematical treatment) or weighted using an erythemal response function [84]. Since skin sensitivity to UV is wavelength dependent, the erythemal response function has been developed in order to weight the wavelength effect and provide a single radiant exposure value, which can be directly corre-

Table 1. ^{1}H chemical shifts (δ, ppm) of *trans* and *cis-ortho*-methoxycinnamic acid in DMSO-d_6.

	trans-OMCA (δ, ppm)		*cis*-OMCA (δ, ppm)	
	Experimental	Calculated	Experimental	Calculated
H2	6.54	6.16	5.97	6.14
H3	7.86	8.04	7.02	7.62
H4	7.70	7.66	7.49	7.66
H5	7.02	7.02	6.93	7.02
H6	7.44	7.49	7.35	7.49
H7	7.11	7.07	7.04	7.10

OMCA: *Ortho*-methoxycinnamic acid.

Table 2. Parameters affecting the nanoparticle aspect ratio.

	AuNRs	AuNWs
pH	+ +	– – –
OMCA redox behavior	–	=
Micelle shape	=	=
Overall effect	+	– – –

+, –, =: Increasing, decreasing and no effect on nanoparticle aspect ratio.
OMCA: *Ortho*-methoxycinnamic acid.

lated to the biological impact [85,86]. Radiant exposure can be expressed in different units, such as energy per surface unit (J/m^2), standard erythemal dose (erythemally weighted radiant exposure unit, equivalent to 100 J/m^2) or minimal erythemal dose (minimal UVR dose to produce detectable erythema in a specific skin type).

Interestingly, just a small fraction of UV light irradiated by the sun reaches earth surface, that is, UVC (100–280 nm) is completely absorbed by atmospheric oxygen and ozone, while UVB (290–315 nm) is partially blocked and UVA (315–400 nm) weakly attenuated [85]. Therefore, when the spectra of erythemal response function and sun irradiance at earth's surface are superimposed, the overlapped area is defined as the biologically active UVR (Figure 10), which is a range of atmosphere-penetrating wavelengths that can induce erythema [85,86].

We propose using the UV-dependent growth of anisotropic nanoparticles in photoresponsive fluids as

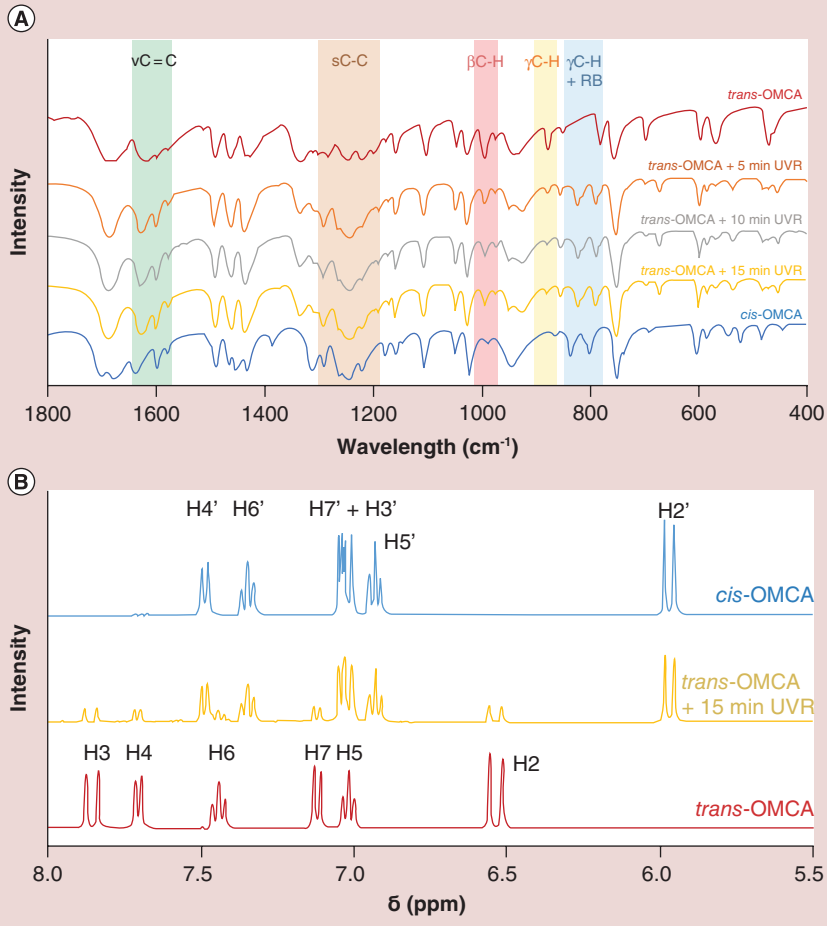

Figure 9. (A) FTIR spectra of *cis*-OMCA and *trans*-OMCA after being irradiated with UV light for 0, 5, 10 or 15 min. **(B)** ^{1}H-NMR spectra of *cis*-OMCA and *trans*-OMCA before and after being irradiated for 15 min in DMSO-d_6.
FTIR: Fourier transform IR; OMCA: *Ortho*-methoxycinnamic acid.

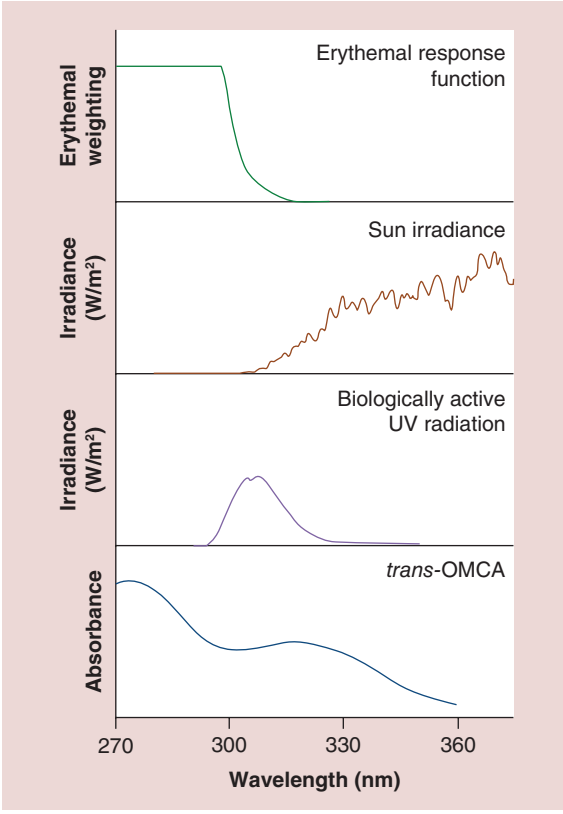

Figure 10. Spectra of erythemal response function (green) [85], sun irradiance at earth's surface (orange) [54], biologically active UV radiation (purple) [85] and *trans-ortho*-methoxycinnamic acid absorbance (blue).

plasmonic nanosensor for UV exposure measurement. The CTAB / *trans*-OMCA system presents several advantages: a) it absorbs in the range of both erythemal response function and biological active UVR (Figure 10); b) it can tune the morphology of AuNR and AuNW under UV irradiation; OMCA photoisomerization is irreversible. AuNRs were chosen for the sensing application over AuNWs, since their L-LSPR band is found in an easier wavelength range to measure (i.e., AuNW L-LSPR band can shift beyond 1000 nm). The growth solutions were irradiated with solar-simulated radiation for different periods of time before the synthesis of the rods. Figure 11A plots the absorbance spectra of the rods grown in those solutions. The L-LSPR band shifts from 813 to 859 nm after 80 min of irradiation, which is in agreement with the previous results presented in this paper. Figure 11B presents a calibration curve built by plotting the ratio between the two LSPR bands (A_L/A_T) with two horizontal axes, the nonerythemally weighted UV radiant exposure (J/m²) and the erythemally weighted standard erythema dose (units). Finally, the sensor dynamic range can be divided in minimal erythemal dose ranges depending on skin-type sensitivity. This allows predicting the potential skin damage of a specific radiant exposure. Thus, the system can be used not only as a sensor for UV exposure but also as prevention tool against erythema.

Conclusion

We have demonstrated that the physicochemical changes induced by UVR on a photoresponsive fluid

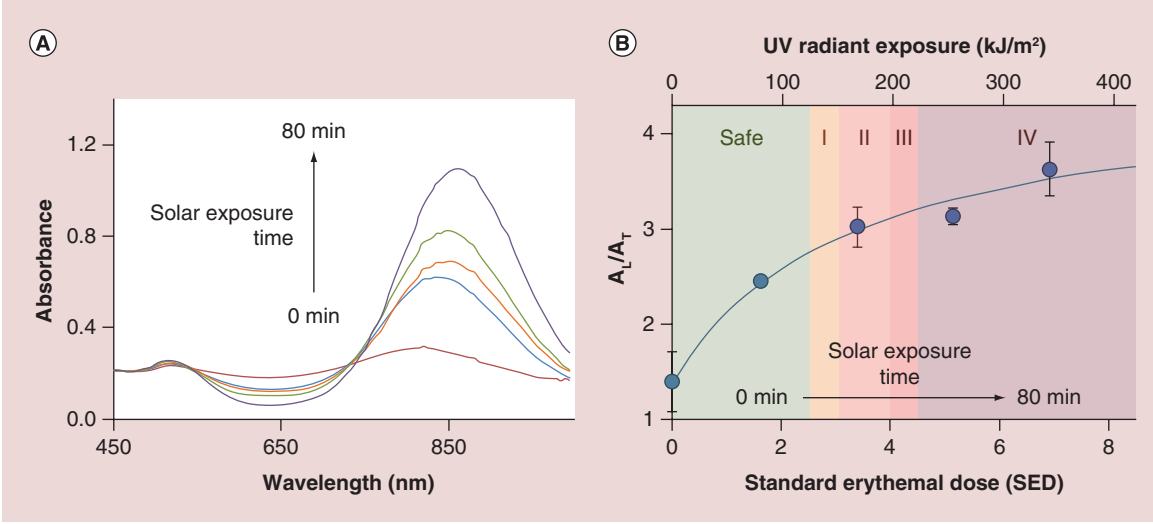

Figure 11. (A) Absorbance spectra of AuNRs grown in the photoresponsive fluid after 0, 20, 40, 60 and 80 min of solar simulated irradiation. **(B)** Variation of the ratio between the AuNR longitudinal (A_L) and transversal (A_T) LSPR bands as a function of nonweighted UV radiant exposure and standard erythemal dose. The graph is divided in areas based on the exposure biological effect: harmless exposures (green) and erythema-causing exposures to skin type I (orange), type II (pink), type III (red) and type IV (dark red).
A_L: AuNR longitudinal; A_T: AuNR transversal.

affect the growth of anisotropic gold nanoparticles, that is, nanorods and nanoworms. The as-prepared nanoparticles' dimensions, plasmon band position and intensity are highly dependent on the UV irradiation. Interestingly, opposite phenomena are observed in the tuning of AuNR and AuNW. While the aspect ratio of the rods increases upon irradiating the photoresponsive fluid with UVR and the L-LSPR band redshifts and increases in intensity, the same irradiation decreases the nanoworm dimensions and blueshifts its L-LSPR band. This distinctive behavior is on account of two factors: the pH change induced by the photoisomerization and the distinct reduction behavior of OMCA isomers. The pH plays a major role on the redox behavior of ascorbic acid, which controls the growth speed and final particle dimensions. Based on those findings, we have developed a plasmonic nanosensor for UV exposure. It is an *in situ* growth sensor that quantifies UV exposure when nanoparticles are synthesized. In this sensor, the UV exposure values can be correlated to the minimal UV-dose necessary to develop erythema. Thus, the growth of anisotropic nanoparticles in the photoresponsive fluid can be used not just as a plasmonic sensor but sunlight-disease prevention tool. Finally, this assay further reinforces the breakthrough strategy of combining both synthesis and sensing steps, while avoiding postsynthesis functionalization and enzyme-based nanoparticle growth, often used in other *in situ* growth sensors.

Supplementary data

To view the supplementary data that accompany this paper please visit the journal website at: www.futuremedicine.com/doi/full/10.2217/nnm-2016-0191

Financial & competing interests disclosure

RM Pallares thanks UCL and A*STAR for his PhD studentship. X Su thanks A*STAR JCO funding 14302FG096. NTK Thanh thanks the Royal Society for her Royal Society University Research Fellowship and EPSRC (grant no. EP/M015157/1) for the financial support. The authors have no other relevant affiliations or financial involvement with any organization or entity with a financial interest in or financial conflict with the subject matter or materials discussed in the manuscript apart from those disclosed.

No writing assistance was utilized in the production of this manuscript.

Executive summary

Objective

- Apply the UV-dependent growth of anisotropic gold nanoparticles in photoresponsive fluids for UV exposure sensing and erythema prediction.

Methods

- Photoresponsive solutions were irradiated in a UV chamber or solar simulation system during different exposure times.
- The irradiated fluids were used as growth solutions for the synthesis of gold nanorods or gold nanoworms.
- The morphology and optical properties of the resulting nanoparticles were characterized by spectroscopy and microscopy.

Results & discussion

- The UV irradiation induces changes on the fluid's physicochemical properties, which tailor the dimensions and optical properties of the resulting nanoparticles.
- The direct dependence between the nanoparticles' localized surface plasmon resonance and UV irradiation, renders the system to be useful as an *in situ* growth sensor for UV exposure.
- The sensing method is expanded to erythema prediction tool by correlating the measured UV exposure levels and the minimal dose to produce erythema.

Conclusion

- A novel plasmonic nanosensing technique for UV exposure and sunlight diseases prevention has been developed by combining a UV responsive fluid and anisotropic gold nanoparticles.
- This design reinforces the *in situ* growth sensing strategy, where the anisotropic nanoparticles are synthesized and used for sensing purpose at the same time.

References

Papers of special note have been highlighted as: • of interest; •• of considerable interest

1 Huang X, Jain PK, El-Sayed IH, El-Sayed MA. Plasmonic photothermal therapy (PPTT) using gold nanoparticles. *Lasers Med. Sci.* 23(3), 217–228 (2008).

2 Kennedy LC, Bickford LR, Lewinski NA *et al.* A new era for cancer treatment: gold-nanoparticle-

mediated thermal therapies. *Small* 7(2), 169–183 (2011).

3 Huff TB, Tong L, Zhao Y, Hansen MN, Cheng J-X, Wei A. Hyperthermic effects of gold nanorods on tumor cells. *Nanomedicine* 2(1), 125–132 (2007).

4 Alkilany AM, Thompson LB, Boulos SP, Sisco PN, Murphy CJ. Gold nanorods: their potential for photothermal therapeutics and drug delivery, tempered by the complexity of their biological interactions. *Adv. Drug Deliv. Rev.* 64(2), 190–199 (2012).

5 Jain PK, Huang X, El-Sayed IH, El-Sayed MA. Noble metals on the nanoscale: optical and photothermal properties and some applications in imaging, sensing, biology, and medicine. *Acc. Chem. Res.* 41(12), 1578–1586 (2008).

• **Comprehensive review of the sensing and biomedical applications of noble metal nanoparticles.**

6 Kim C, Favazza C, Wang L V. *In vivo* photoacoustic tomography of chemicals: high-resolution functional and molecular optical imaging at new depths. *Chem. Rev.* 110(5), 2756–2782 (2010).

7 Stender AS, Marchuk K, Liu C *et al.* Single cell optical imaging and spectroscopy. *Chem. Rev.* 113(4), 2469–2527 (2013).

8 Wang H, Huff TB, Zweifel DA *et al. In vitro* and *in vivo* two-photon luminescence imaging of single gold nanorods. *Proc. Natl Acad. Sci. USA* 102(44), 15752–15756 (2005).

9 Vigderman L, Khanal BP, Zubarev ER. Functional gold nanorods: synthesis, self-assembly, and sensing applications. *Adv. Mater.* 24(36), 4811–4841 (2012).

• **Comprehensive review of the sensing applications of gold nanorods.**

10 Yu C, Irudayaraj J. Multiplex biosensor using gold nanorods. *Anal. Chem.* 79(2), 572–579 (2007).

11 Stewart ME, Anderton CR, Thompson LB *et al.* Nanostructured plasmonic sensors. *Chem. Rev.* 108(2), 494–521 (2008).

12 Ghosh SK, Pal T. Interparticle coupling effect on the surface plasmon resonance of gold nanoparticles: from theory to applications. *Chem. Rev.* 107(11), 4797–4862 (2007).

13 Link S, El-Sayed M. Size and temperature dependence of the plasmon absorption of colloidal gold nanoparticles. *J. Phys. Chem. B.* 103(21), 4212–4217 (1999).

14 El-Sayed MA. Some interesting properties of metals confined in time and nanometer space of different shapes. *Acc. Chem. Res.* 34(4), 257–264 (2001).

15 Pérez-Juste J, Pastoriza-Santos I, Liz-Marzán LM, Mulvaney P. Gold nanorods: synthesis, characterization and applications. *Coord. Chem. Rev.* 249(17–18 SPEC. ISS.), 1870–1901 (2005).

16 Huang X, Neretina S, El-Sayed MA. Gold nanorods: from synthesis and properties to biological and biomedical applications. *Adv. Mater.* 21(48), 4880–4910 (2009).

17 Nehl CL, Liao H, Hafner JH. Optical properties of star-shaped gold nanoparticles. *Nano Lett.* 6(4), 683–688 (2006).

18 Senthil KP, Pastoriza-Santos I, Rodríguez-González B, Javier García de Abajo F, Liz-Marzán LM. High-yield synthesis and optical response of gold nanostars. *Nanotechnology* 19(1), 15606 (2008).

19 Khoury CG, Vo-Dinh T. Gold nanostars for surface-enhanced Raman scattering: synthesis, characterization and optimization. *J. Phys. Chem. C* 112(48), 18849–18859 (2008).

20 West JL, Halas NJ. Applications of nanotechnology to biotechnology. *Curr. Opin. Biotechnol.* 11(2), 215–217 (2000).

21 Loo C, Hirsch L, Lee M-H *et al.* Gold nanoshell bioconjugates for molecular imaging in living cells. *Opt. Lett.* 30(9), 1012–1014 (2005).

22 Shankar SS, Rai A, Ankamwar B, Singh A, Ahmad A, Sastry M. Biological synthesis of triangular gold nanoprisms. *Nat. Mater.* 3(7), 482–488 (2004).

23 Chandran SP, Chaudhary M, Pasricha R, Ahmad A, Sastry M. Synthesis of gold nanotriangles and silver nanoparticles using aloevera plant extract. *Biotechnol. Prog.* 22(2), 577–583 (2006).

24 Ahmed W, Glass C, van Ruitenbeek JM. Facile synthesis of gold nanoworms with a tunable length and aspect ratio through oriented attachment of nanoparticles. *Nanoscale* 6(21), 13222–13227 (2014).

25 Grzelczak M, Pérez-Juste J, Mulvaney P, Liz-Marzán LM. Shape control in gold nanoparticle synthesis. *Chem. Soc. Rev.* 37(9), 1783–1791 (2008).

26 Pallares RM, Su X, Lim SH, Thanh NTK. Fine-tuning of gold nanorod dimensions and plasmonic properties using the Hofmeister effects. *J. Mater. Chem. C* 4(1), 53–61 (2016).

27 Chu Z, Dreiss CA, Feng Y. Smart wormlike micelles. *Chem. Soc. Rev.* 42(17), 7174–7203 (2013).

• **Comprehensive review of smart fluids and their potential applications.**

28 Nikoobakht B, El-Sayed MA. Preparation and growth mechanism of gold nanorods (NRs) using seed-mediated growth method. *Chem. Mater.* 15(10), 1957–1962 (2003).

29 Ye X, Jin L, Caglayan H *et al.* Improved size-tunable synthesis of monodisperse gold nanorods through the use of aromatic additives. *ACS Nano* 6(3), 2804–2817 (2012).

30 Feng Y, Chu Z, Dreiss CA. Light-responsive wormlike micelles. In: *Smart Wormlike Micelles*. Springer Berlin Heidelberg, Berlin, Heidelberg, Germany, 29–40 (2015).

31 Sakai H, Orihara Y, Kodashima H *et al.* Photoinduced reversible change of fluid viscosity. *J. Am. Chem. Soc.* 127(39), 13454–13455 (2005).

32 Ketner AM, Kumar R, Davies TS, Elder PW, Raghavan SR. A simple class of photorheological fluids: surfactant solutions with viscosity tunable by light. *J. Am. Chem. Soc.* 129(6), 1553–1559 (2007).

33 Kim F, Song JH, Yang P. Photochemical synthesis of gold nanorods. *J. Am. Chem. Soc.* 124(48), 14316–14317 (2002).

34 Miranda OR, Ahmadi TS. Effects of intensity and energy of CW UV light on the growth of gold nanorods. *J. Phys. Chem. B.* 109(33), 15724–15734 (2005).

35 Niidome Y, Nishioka K, Kawasaki H, Yamada S. Rapid synthesis of gold nanorods by the combination of chemical

reduction and photoirradiation processes; morphological changes depending on the growing processes. *Chem. Commun.* (18), 2376–2377 (2003).

36 Elghanian R, Storhoff JJ, Mucic RC, Letsinger RL, Mirkin CA. Selective colorimetric detection of polynucleotides based on the distance-dependent optical properties of gold nanoparticles. *Science* 277(5329), 1078–1081 (1997).

37 Kim Thanh NT, Rosenzweig Z. Development of an aggregation-based immunoassay for anti-protein A using gold nanoparticles. *Anal. Chem.* 74(7), 1624–1628 (2002).

38 Lee JS, Han MS, Mirkin CA. Colorimetric detection of mercuric ion (Hg^{2+}) in aqueous media using DNA-functionalized gold nanoparticles. *Angew. Chemie Int. Ed. Engl.* 46(22), 4093–4096 (2007).

39 Liu J, Lu Y. Preparation of aptamer-linked gold nanoparticle purple aggregates for colorimetric sensing of analytes. *Nat. Protoc.* 1(1), 246–252 (2006).

40 Su X, Kanjanawarut R. Control of metal nanoparticles aggregation and dispersion by PNA and PNA–DNA complexes, and its application for colorimetric DNA detection. *ACS Nano* 3(9), 2751–2759 (2009).

41 Pallares RM, Kong SL, Ru TH, Thanh NTK, Lu Y, Su X. A plasmonic nanosensor with inverse sensitivity for circulating cell-free DNA quantification. *Chem. Commun.* 51(77), 14524–14527 (2015).

42 Kanjanawarut R, Su X. Colorimetric detection of DNA using unmodified metallic nanoparticles and peptide nucleic acid probes. *Anal. Chem.* 81(15), 6122–6129 (2009).

43 de la Rica R, Stevens MM. Plasmonic ELISA for the ultrasensitive detection of disease biomarkers with the naked eye. *Nat. Nanotechnol.* 8(9), 1759–1764 (2012).

•• **First plasmonic ELISA sensor ever developed. It is based on the enzyme-selective growth of different gold nanoparticle morphologies.**

44 Cecchin D, de la Rica R, Bain RES, Finnis MW, Stevens MM, Battaglia G. Plasmonic ELISA for the detection of gp120 at ultralow concentrations with the naked eye. *Nanoscale* 6(16), 9559–9562 (2014).

45 Nie XM, Huang R, Dong CX, Tang LJ, Gui R, Jiang JH. Plasmonic ELISA for the ultrasensitive detection of *Treponema pallidum*. *Biosens. Bioelectron.* 58, 314–319 (2014).

46 Coronado-Puchau M, Saa L, Grzelczak M, Pavlov V, Liz-Marzán LM. Enzymatic modulation of gold nanorod growth and application to nerve gas detection. *Nano Today* 8(5), 461–468 (2013).

•• **Sensing of nerve gas analogous by enzymatically tuning the morphology of gold nanorods.**

47 Mansoori GA, Mohazzabi P, McCormack P, Jabbari S. Nanotechnology in cancer prevention, detection and treatment: bright future lies ahead. *World Rev. Sci. Technol. Sustain. Dev.* 4(2/3), 226–257 (2007).

48 Lucas RM. An epidemiological perspective of ultraviolet exposure – public health concerns. *Eye Contact Lens.* 37(4), 168–175 (2011).

• **Extensive perspective of UV radiation effect on human body and sunlight-related diseases.**

49 Farr PM, Besag JE, Diffey BL. The time course of UVB and UVC erythema. *J. Invest. Dermatol.* 91(5), 454–457 (1988).

50 Young AR. Tanning devices-fast track to skin cancer? *Pigment Cell Res.* 17(1), 2–9 (2004).

51 Matsumura Y, Ananthaswamy HN. Short-term and long-term cellular and molecular events following UV irradiation of skin: implications for molecular medicine. *Expert Rev. Mol. Med.* 4, 1–22 (2002).

52 Vink AA, Roza L. Biological consequences of cyclobutane pyrimidine dimers. *J. Photochem. Photobiol. B Biol.* 65(2–3), 101–104 (2001).

53 Thacher TD, Clarke BL. Vitamin D insufficiency. *Mayo Clin. Proc.* 86(1), 50–60 (2011).

54 ASTM International. ASTM G173–03. Stand. Tables Ref. Sol. Spectr. Irradiances Direct Norm. Hemispherical 37° Tilted Surf (2012). http://rredc.nrel.gov/solar/spectra/am1.5/

55 Jana NR, Gearheart L, Murphy CJ. Wet chemical synthesis of high aspect ratio cylindrical gold nanorods. *J. Phys. Chem. B.* 105(19), 4065–4067 (2001).

56 Rawat KA, Kailasa SK. 4-Amino nicotinic acid mediated synthesis of gold nanoparticles for visual detection of arginine, histidine, methionine and tryptophan. *Sensors Actuators B Chem.* 222, 780–789 (2016).

57 Kasibabu BSB, Bhamore JR, D'souza SL, Kailasa SK. Dicoumarol assisted synthesis of water dispersible gold nanoparticles for colorimetric sensing of cysteine and lysozyme in biofluids. *RSC Adv.* 5(49), 39182–39191 (2015).

58 Rawat KA, Kailasa SK. 2, 3,4-Trihydroxy benzophenone as a novel reducing agent for one-step synthesis of size-optimized gold nanoparticles and their application in colorimetric sensing of adenine at nanomolar concentration. *RSC Adv.* 6(14), 11099–11108 (2016).

59 Rawat KA, Kailasa SK. Visual detection of arginine, histidine and lysine using quercetin-functionalized gold nanoparticles. *Microchim. Acta* 181(15), 1917–1929 (2014).

60 Rao GVN. Importance of optimizing X-ray beam optics for high-quality data acquisition using conventional X-ray diffraction techniques. In: *Advanced X-Ray Techniques In Research And Industry*. Singh AK (Ed.). IOS Press, Amsterdam, The Netherlands, 562 (2005).

61 Bors W, Buettner GR. The vitamin C radical and its reactions. In: *Vitamin C in health and disease*. Packer L (Ed.). Marcel Dekker, Inc., NY, USA, 75–94 (1997).

62 Wei Q, Ji J, Shen J. pH controlled synthesis of high aspect-ratio gold nanorods. *J. Nanosci. Nanotechnol.* 8(11), 5708–5714 (2008).

63 Kim YG, Oh SK, Crooks RM. Preparation and characterization of 1–2 nm dendrimer-encapsulated gold nanoparticles having very narrow size distributions. *Chem. Mater.* 16(1), 167–172 (2004).

64 Giacomelli C, Ckless K, Galato D, Miranda FS, Spinelli A. Electrochemistry of caffeic acid aqueous solutions with pH 2.0 to 8.5. *J. Braz. Chem. Soc.* 13(3), 332–338 (2002).

65 Amorati R, Pedulli GF, Cabrini L, Zambonin L, Landi L. Solvent and pH effects on the antioxidant activity of

caffeic and other phenolic acids. *J. Agric. Food Chem.* 54(8), 2932–2937 (2006).

66 Gil E de S, Enache TA, Oliveira-Brett AM. Redox behaviour of verbascoside and rosmarinic acid. *Comb. Chem. High Throughput Screen.* 16(2), 92–97 (2013).

67 Smith BC. *Infrared Spectral Interpretation: A Systematic Approach*. CRC press, FL, USA (1988).

68 Arjunan V, Anitha R, Thenmozhi S, Marchewka MK, Mohan S. Potential energy profile, structural, vibrational and reactivity descriptors of trans–2–methoxycinnamic acid by FTIR, FT-Raman and quantum chemical studies. *J. Mol. Struct.* 1113, 42–54 (2016).

69 Arjunan V, Anitha R, Marchewka MK, Mohan S, Yang H. Conformational, structural, vibrational, electronic and quantum chemical investigations of cis-2-methoxycinnamic acid. *J. Mol. Struct.* 1080, 122–136 (2015).

70 Allen SDM, Almond MJ, Bruneel JL, Gilbert A, Hollins P, Mascetti J. Photodimerization of trans-cinnamic acid and its derivatives: a study by vibrational microspectroscopy. *Spectrochim. Acta A Mol. Biomol. Spectrosc.* 56(12), 2423–2430 (2000).

71 Hanai K, Kuwae A, Takai T, Senda H, Kunimoto KK. Comparative vibrational and NMR study of cis-cinnamic acid polymorphs and trans-cinnamic acid. *Spectrochim. Acta A Mol. Biomol. Spectrosc.* 57(3), 513–519 (2001).

72 Haynes W. M. *CRC Handbook of Chemistry and Physics (93rd Edition)*. CRC Press, FL, USA (2012).

73 Grodzińska-Zachwieja Z. Optimization of the separation of cis- and trans-hydroxycinnamic acids by reversed-phase thin-layer chromatography. *J. Chromatogr. A* 241(1), 217–222 (1982).

74 Yaws CL. *The Yaws Handbook of Physical Properties for Hydrocarbons and Chemicals: Physical Properties for More Than 41,000 Organic and Inorganic Chemical Compounds*. Gulf Publishing Company, TX, USA (2015).

75 Sandris C. Sur l'isomerie geometrique d'acides α,β-ethyleniques – I. *Tetrahedron.* 24(9), 3569–3582 (1968).

76 Khan MMT, Martell AE. Metal ion and metal chelate catalyzed oxidation of ascorbic acid. *J. Am. Chem. Soc.* 89(16), 4176–4185 (1967).

77 Khan MMT, Martell AE. Kinetics of metal ion and metal chelate catalyzed oxidation of ascorbic acid. IV. Uranyl ion catalyzed oxidation. *J. Am. Chem. Soc.* 91(17), 4668–4672 (1969).

78 Gramlich G, Zhang J, Nau WM. Increased antioxidant reactivity of vitamin C at low pH in model membranes. *J. Am. Chem. Soc.* 124(38), 11252–11253 (2002).

79 Makote RD, Chatterjee C. Kinetics and mechanism of oxidation of ascorbic acid by cobalt (III) amino polycarboxylato complexes in weakly basic media. *Indian J. Chem. Sect. A.* 38, 783–791 (1999).

80 Njus D, Jalukar V, Zu J, Kelley PM. Concerted proton-electron transfer between ascorbic acid and cytochrome b561. *Am. J. Clin. Nutr.* 54(Suppl. 6), S1179–S1183 (1991).

81 Friedman M, Jürgens HS. Effect of pH on the stability of plant phenolic compounds. *J. Agric. Food Chem.* 48(6), 2101–2110 (2000).

82 Vairamani M, Saraswathi M, Rao GKV. Evidence for metal surface catalysed reduction of unsaturated carboxylic acids under negative ion chemical ionization. *Org. Mass Spectrom.* 25(5), 274–276 (1990).

83 Connors KA, Lipari JM. Effect of cycloamyloses on apparent dissociation constants of carboxylic acids and phenols: equilibrium analytical selectivity induced by complex formation. *J. Pharm. Sci.* 65(3), 379–383 (1976).

84 Lucas R, McMichael T, Smith W, Armstrong B. *Global Burden Of Disease From Solar Ultraviolet Radiation. Environmental Burden of Disease Series*. WHO, Geneva, Switzerland, 4–5 (2006).

85 Madronich S, McKenzie RL, Björn LO, Caldwell MM. Changes in biologically active ultraviolet radiation reaching the Earth's surface. *J. Photochem. Photobiol. B Biol.* 46(1–3), 5–19 (1998).

86 McKenzie R, Smale D, Kotkamp M. Relationship between UVB and erythemally weighted radiation. *Photochem. Photobiol. Sci.* 3(3), 252–256 (2004).